

PAPER

# Nebulized jet-based printing of bio-electrical scaffolds for neural tissue engineering: a feasibility study

To cite this article: Miriam Seiti *et al* 2020 *Biofabrication* 12 025024

View the [article online](#) for updates and enhancements.



**SUNP BIOTECH**

**BIOMAKER** EASY-TO-USE  
AFFORDABLE  
CUSTOMIZABLE  
FULLY FEATURED

BIOPRINTING.  
LIKE NEVER  
BEFORE.

LEARN  
MORE

# Biofabrication



## PAPER

# Nebulized jet-based printing of bio-electrical scaffolds for neural tissue engineering: a feasibility study

RECEIVED  
13 September 2019

REVISED  
6 January 2020

ACCEPTED FOR PUBLICATION  
30 January 2020

PUBLISHED  
4 March 2020

Miriam Seiti<sup>1,2,4</sup> , Paola Ginestra<sup>2</sup>, Rosalba Monica Ferraro<sup>3</sup>, Elisabetta Ceretti<sup>2</sup> and Eleonora Ferraris<sup>1</sup>

<sup>1</sup> Department of Mechanical Engineering, Campus De Nayer, KU Leuven, Belgium

<sup>2</sup> Department of Mechanical Engineering, University of Brescia, Brescia, Italy

<sup>3</sup> Department of Molecular and Translational Medicine, 'Angelo Nocivelli' Institute of Molecular Medicine, University of Brescia, Brescia, Italy

<sup>4</sup> Author to whom any correspondence should be addressed.

E-mail: [miriam.seiti@kuleuven.be](mailto:miriam.seiti@kuleuven.be)

**Keywords:** neural tissue engineering, additive manufacturing, printed electronics

## Abstract

In this paper we investigate the application of a direct writing technique for printing conductive patterns onto a biocompatible electrospun-pyrolysed carbon-fibre-based substrate. The result is a first study towards the production of bio-electrical scaffolds that could be used to enhance the promotion of efficient connections among neurons for *in vitro* studies in the field of neural tissue engineering. An electrospinning process is employed for production of the materials derived from the precursor polyacrylonitrile, in which the embedding of carbon nanotubes (CNTs) is also investigated. Subsequently, the methodology of research into suitable parameters for the printed electronics, using a commercial silver nanoparticle ( $\phi_{\text{avg,particle size}} \sim 100$  nm) ink, is described. The results show values of  $2 \Omega \text{ cm}$  for the resistivity of the carbon-fibre materials and conductive printed lines of resistance  $\sim 50 \Omega$  on glass and less than  $\sim 140 \Omega$  on carbon-fibre samples. Biocompatibility results demonstrate the possibility of using electrospun-pyrolysed mats, also with embedded CNTs, as potential neural substrates for spatially localized electrical stimulation across a tissue. In addition, the data concerning the potential toxicity of silver suspensions are in accordance with the literature, showing a dose-dependent behaviour. This work is a pioneering feasibility study of the use of the flexible and versatile printed electronic approach, combined with engineered biocompatible substrates, to realize integrated bio-electrical scaffolds for *in vitro* neural tissue engineering applications.

## 1. Introduction

Every year neuro-degenerative diseases (e.g. Alzheimer's, Parkinson's) have direct consequences for millions of people. Nine out of ten individuals over the age of 80 years will probably suffer from a brain disorder, which account for  $\sim 35\%$  of all human diseases [1].

Because of the poor regenerative capacity of the central nervous system [2], neural tissue engineering investigates the design and production of scaffolds to restore the functions of injured neural tissues [3]. Scaffolds act as a means of mimicking the complex *in vivo* neural environment, focusing on different guidance cues such as molecular, electrical, topographical or chemical ones [2]. In the ideal case, a combination of these cues will produce a synthetic fabric similar to the

natural extracellular matrix (ECM), which governs the physiology of neural cells [4].

Over the last century, a large number of biocompatible materials were developed using several techniques. Boni *et al* [5] reviewed different natural and synthetic polymers, with specifications aimed at emphasizing adhesion, growth, orientation, proliferation and differentiation of different types of neuronal and neural cells.

Among the techniques most often used to produce biocompatible scaffolds, electrospinning is well known to produce suitable scaffolds for adhesion, proliferation and extension of neurons [6]. This technique is able to electrospin various materials including biodegradable, non-degradable and natural materials [7]. Its main advantage is the ability to produce non-woven polymer mats consisting of nanofibres in a versatile, flexible and

affordable way [8]. Fibre diameters can range from several nanometres to a few micrometres, and the possibility of controlling their desired viscosity and conductivity of the solution facilitates the production of engineered neural scaffolds. Specifically, electrospun nanofibres can be assembled into scaffolds by manipulating their morphology, alignment, stacking and/or folding behaviour [9]. As reported by Xie *et al* [10], anisotropic fibre arrangements show a effective cues to direct and enhance neurite outgrowth than isotropic materials such as hydrogels. For instance, cell differentiation and enhancement of neurite outgrowth have been tested on aligned poly(L-lactic acid) nano/microfibrous scaffolds [11]. In addition, neural bio-electrical properties and synaptic activities can be modulated by material–neuron interactions, when substrates are also characterized by a high level of electrical conductivity. Hence, the embedding of conductive nanomaterials in neural interfaces has also been found to promote efficient connections among cells and preserve normal or even enhanced neuronal activities, after stem cell differentiation. Among these materials, carbon-based nanomaterials such as graphene films [12], three-dimensional graphene foams [13], reduced graphene oxide with poly(3,4-ethylenedioxythiophene) (PEDOT) [14], carbon nanotubes (CNTs) [15], CNT ropes [16], multi-walled CNTs (MWCNTs) [17] and MWCNTs with a PEGDA polymer [18] have been explored for these applications, with promising outcomes.

Bio-electricity mostly regulates cell behaviours and biological functions (cell adhesion, proliferation and migration) during tissue regeneration. The application of an electrical field can support this process in *in vitro* applications [19]. In this context, neural engineering aims to study neuronal networks using electrical stimulation (ES) impulses through the development of an interface between electronic devices and living neural tissue [20]. ES is indeed an efficient approach to stimulate and record the activities of neural cells [21]. An applied electric field (or an electric current) can influence the direction and proliferation of neurite growth [2] if the cell membrane achieves certain action potentials (rest potential  $\sim -70$  mV), that would cause the activation of ionic channels.

Spira *et al* [22] described the commonest methodologies for ES, such as (i) intracellular stimulation and signal recording by means of a sharp needle-shaped electrode (invasive technique), (ii) extracellular stimulation and signal recording via substrate-integrated micro-electrode arrays (MEAs), and (iii) ES followed by optical imaging of extrinsic fluorescent indicators. More specifically, MEAs are the current technology for long-term studies of electrophysiological phenomena. However, they still do not offer the same capability for correct fluid exchange among the cells or a three-dimensional surface area for *in vitro* cultures. Moreover, current solutions are mostly available on rigid substrates (Young's modulus,  $E$ , of the order of GPa), which do not represent the

ideal cellular soft environment for unaltered biological activity ( $E$  of the neural biological carrier ideally between 0.1 and 10 kPa) [23]. Instead, ES could directly be applied to ECM-mimicking scaffolds, such as electrospun conductive polyaniline/poly( $\epsilon$ -caprolactone)/gelatin nanofibres [24], with major benefits but possibly lower recording accuracy.

In this scenario, printed electronics (PE) could be a novel solution to merge tissue engineering and additive manufacturing for the generation of ES spatially localized across a fabric, with possible recording of cellular activity. There are potential applications for PE in regenerative medicine for neuronal studies, and much more. More specifically, printing of electronics is a set of printing techniques specializing in PE circuits on several substrates and for a wide range of applications. Among these are nebulized jet-based techniques of the direct writing nozzle-based category, a macro-area of additive manufacturing. These have a competitive advantage for the semiconductor industry, thanks to the ease of designing and prototyping cost-effective multi-material/multi-functional structures, without material wastage or the requirement for masks at micrometre or nanometre resolution [25]. Moreover, a broad range of customized PEs, such as parts of light-emitting diodes (LEDs) [26] and organic LEDs [27], solar cells [28], sensors [29], antennas [30], transistors [31], capacitors [32] and for applications in the biomedical field [33], have already been validated on various planar and non-planar substrates, rigid and flexible supports, textile and paper foils. [34, 35]. The key advantages of nebulized jet manufacturing over other jet-based techniques (e.g. ink-jet printing) are summarized in the following points. (i) A broad range of printable (nano-) inks [36], with viscosity from 1 up to 1000 mPa s and particle size  $<0.5 \mu\text{m}$  [25]. Typical examples include nano-metal inks (Ag, Au, Cu, etc), conductive polymer suspensions [e.g. PEDOT:polystyrene sulphonate (PSS), polypyrrole, etc], semiconductor, carbon-based and dielectric solutions (e.g. epoxy, polyimide, etc) or biological substances (such as collagen [37], bovine serum albumin protein, DNA and enzymes [38]). (ii) Printability on various substrates [glass, FR4, polydimethylsiloxane (PDMS), thermoplastic polyurethane foils, textile, papers, etc], including *free-formed* supports, thanks to the variable stand-off distance (between 1–5 mm), i.e. the distance between the tip of the print nozzle and the substrate. (iii) High accuracy (feature sizes ranging from  $\sim 10 \mu\text{m}$  to a few mm and thin layer deposition starts from  $\sim 100 \text{nm}$  [39]).

In this study, we investigate the printing of electrical patterns, using a nebulized jet-based technique, on the top of biocompatible electrospun-pyrolysed polymeric scaffolds to generate a bio-electrical scaffold for neural tissue engineering applications. More specifically, in the next sections we report the fabrication of fibrous scaffolds and the identification of suitable parameters for printing conductive silver patterns on

these substrates, along with biocompatible analyses and circuit validation.

The fibrous scaffolds were electrospun using a solution containing polyacrylonitrile (PAN), a versatile biocompatible polymer obtained from the polymerization of acrylonitrile, which is conventionally used in biomedical applications such as implantation, drug delivery and dialysis membranes [40].

The embedding of conductive nanoparticles, such as CNTs, was also analysed. CNTs have attracted considerable attention in the past decade as material candidates for nerve/neural tissue engineering applications [41, 42]. Despite concerns about their reported relative cytotoxicity [41, 43, 44], each case has to be considered according to the CNT concentration, size, shape and direction in the solution, along with any bio-functionalization and post-fabrication treatments [44, 45]. CNTs usually show high electrical conductivity ( $10^4 \text{ S cm}^{-2}$ ), excellent mechanical properties [45, 46] and structural and chemical (surface functionalization) enhancements with their incorporation into polymers and hydrogel scaffolds [18, 42, 45], and morphological affinity to neurites [41, 47]. Various studies have revealed an increase in adhesion, proliferation and increase in neural activity, such as successful control the characteristics of neurite outgrowth via surface manipulation of CNTs [46] or improving neural signal transfer while supporting dendrite elongation and cell adhesion [15]. In particular, among the different techniques for manipulating CNTs, electrospinning emerges as a powerful method to disperse and align functionalized CNTs [45, 48, 49].

According to the main objective of the paper (namely, a feasibility study on combining the fields of PE and neural tissue engineering), a commonly used PE ink, specifically customized for nebulized jet printing techniques, was selected. It is a commercial silver nanoparticle (AgNP;  $\text{O}_{\text{particle size}} \sim 100 \text{ nm}$ ) ink; AgNP suspensions are, in fact, the most widely adopted engineered inks in PE, due to their high conductivity and printing versatility [50].

It is widely reported in the literature that the biological activity of AgNPs induces cytotoxicity in a complex multi-factorial environment, which is dependent on dose, size, shape, surface coating [51], agglomeration, dissolution rate and time [52]. Specifically, in biological solutions, the AgNP surface can be mainly oxidized by  $\text{O}_2$ , activating the release of  $\text{Ag}^+$  ions, which can interact with nucleic acids, lipid molecules and proteins, causing oxidative stress and damaging several cellular components [53]. On the other hand, to the best of our knowledge, most of the studies on *in vitro* cell cultures, report cytotoxicity of AgNP powders at various concentrations [51, 54–61], with a  $\text{O}_{\text{avg particle size}} \ll 100 \text{ nm}$ , i.e. much smaller than the AgNP ink suspension used in our study ( $\text{O}_{\text{avg,particle size}} \sim 100 \text{ nm}$ ). Accordingly, Johnston *et al* [57] reported that smaller particles have a higher toxic potential than bigger

**Table 1.** Parameters for the electrospinning process.

Parameter	Value
Syringe pump	5 ml with 21-gauge needle
DC voltage	10 kV
Injection flow rate	$1 \text{ ml h}^{-1}$
Needle tip–collector distance	21 mm
Type of collector	Plate of copper covered by an aluminium foil

ones on an equal-mass basis. Furthermore, Alon *et al* found minimum toxic levels of sputtered Ag when  $\text{O}_{\text{avg,particle size}} \sim 120 \text{ nm}$ , most likely due to surface functionalization and a homogeneous production process for Ag-sputtered layers [62]. Therefore, this paper does not just report on a novel technique to realize bio-electrical scaffolds but also provides new insights concerning the use of conductive nanoparticles, such as CNTs and AgNPs, to enhance neural activity.

## 2. Materials and methods

### 2.1. Substrate production and characterization

The scaffolds, on the top of which conductive patterns were printed, are composed of carbon fibres derived from the precursor PAN. CNTs were also embedded in the electrospinning solution, and two substrates, later referred to as PAN and PAN + CNT, were produced in order to investigate the effects of including nano-conductive particles on the final product of polymerization. PAN and PAN + CNT substrates were obtained by electrospinning of a solution of 8 wt% PAN ( $150\,000 \text{ g mol}^{-1}$ ) dissolved in dimethylformamide (DMF). The solution was stirred for 48 h at  $30^\circ\text{C}$ . The PAN + CNT solution was made by dissolving 1 wt% CNTs in DMF (by sonication for 1 h at  $35^\circ\text{C}$ ) and adding PAN in a second step. Subsequently, both materials were electrospun using a 5 ml syringe with a 21-gauge needle on a flat collector composed of one plate of copper, covered by an aluminium foil. Afterwards, the fibres were subjected to thermal stabilization at  $280^\circ\text{C}$  for 6 h and to pyrolysis up to  $1050^\circ\text{C}$  in a controlled atmosphere (table 1, figure 1) [63]. The final fibrous mats were dark coloured, brittle, thin films.

#### 2.1.1. Morphological characterization

Characterization of the fibres was performed using a scanning electron microscope (SEM) under ambient conditions ( $23^\circ\text{C}$ , 50% relative humidity) and 20.00 kV vacuum. Measurements of the average diameter of the fibres were calculated using ImageJ software. For both the PAN and PAN + CNT samples, 120 measurements in different and random spatial regions were taken.

The electron diffraction pattern was analysed using a transmission electron microscope (TEM) to

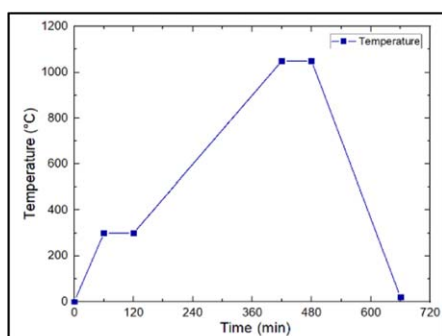


**Figure 1.** The (pre)-carbonization phase in the pyrolysis process: a first pre-carbonization phase from room temperature at 20 °C, with an increase of 4 °C min<sup>-1</sup> for 1 h, followed by another hour at 300 °C. Subsequently, a second increase of 2.5 °C min<sup>-1</sup> for 5 h, followed by the carbonization phase at 1050 °C for 1 h. Finally, a cooling process from 1050 °C to 20 °C over a period of 3 h.

**Table 2.** Properties of the SI-AJ 20X ink. For more details see the ink datasheet [64].

Feature	Description
Printing process	Optimized for aerosol jet <sup>®</sup> printing
Functional material	19.0 wt% silver
Viscosity	7.1 mPa s
Ave. particle size	100 nm
Appearance	Dark-grey colour

detect the degree of graphitization in the nanofibres. In addition, the average crystallite thickness ( $L_c$ ) was measured from the distance between the layers by the fringes.

The material thickness was measured using a Schut micrometer (accuracy  $\pm 2 \mu\text{m}$ ) under ambient conditions.

### 2.1.2. Electrical properties

A four-point measurement was used to detect the sheet resistance of the materials in clean-room conditions (Veeco Instruments Inc., Four Point Probe, model FPP-100). For each material, 15 repetitions on two different samples were recorded.

## 2.2. Ink

In this study, a commercial AgNP solution ink SI-AJ 20X (supplied by AGFA) was used. Table 2 reports the main properties of the ink. The interaction forces between ink particles and substrates (PAN, PAN + CNT and glass) were studied using a sessile drop on a Contact Angle System OCA 15plus for wettability tests under ambient conditions. This is a common test in printing techniques to check the substrate–ink interaction and the adhesion to a particular substrate. A sessile drop of 2  $\mu\text{l}$  was deposited on the substrates via a Nordson 7018339 straight, 25-gauge, 1.5 inch long red dispensing needle. Measurements were recorded automatically and fitted by the

software from the starting point when the drop was deposited on the substrate until the measurement was stable ( $\sim 5$  s).

## 2.3. Printing process

### 2.3.1. Nebula 5X-100 s

The printing process was conducted on a Nebula 5X-100 s, a five-axis home-made nebulized jet-based printer, designed and manufactured at the Advanced Manufacturing Laboratory (AML), Campus De Nayer, KU Leuven, Belgium (figure 2(A)). The machine offers a printing speed in the range of 0–200 mm min<sup>-1</sup>, a stand-off distance of 1–5 mm and a positional accuracy of  $\pm 10 \mu\text{m}$  on the  $z$ -axis and  $\pm 20 \mu\text{m}$  on the  $x$  and  $y$  axes. Typically, conical-shaped nozzles are mounted on the deposition head to ensure jet focusing. In this study, 10 cm<sup>3</sup> Nordson EFD Luer lock nozzles ( $\text{Ø} = 250 \mu\text{m}$  and  $\text{Ø} = 610 \mu\text{m}$ , length 31.6 mm) are employed. The Nebula 5X-100 s is equipped with a pneumatic atomizer for the creation of an aerosol flow at controlled air pressure in the range of 0–5 bar. The aerosol flow subsequently goes in a virtual impactor, which is used to filter the accelerating gas to get a focused beam. A schematic view of the printing process is given in figure 2(B). For a reliable process, the minimum ink level required in the atomizer is  $\sim 3$  ml and the printed line resolution is in the range of 100–300  $\mu\text{m}$ , depending on the particular ink–substrate combination. The printer has been validated on various flat and curved substrates using different silver inks.

### 2.3.2. Experimental printing methodology

Various experimental methodologies were used to identify suitable printing parameters for specific ink–substrate combinations. Experiments were first conducted on glass substrates (from VWR) as a positive control, and then transferred to PAN mats. The glass experiments consisted of a first screening session, of type  $2^k$  ( $k > 0$ ) full factorial design (two levels,  $k = 4$  factors, five repetitions), followed by a greedy algorithm investigation within an adapted process window. The following factors were investigated in the screening session: nozzle diameter  $\text{Ø}$  ( $\mu\text{m}$ ), stand-off distance  $z$  (mm), control pressure  $p$  (bar), print speed  $s$  (mm min<sup>-1</sup>) and number of printed layers  $n$  as shown in table 3.

Based on the results obtained,  $z$  and  $p$  were further investigated in a greedy algorithm investigation. Accordingly, an additional greedy algorithm investigation was conducted on the PAN substrates to fine-tune the best practice combination obtained on glass. Due to the higher wettability (see section 3.2 and figure 7) and the fragility of PAN and PAN + CNTs, 40 layers were printed instead of 10 and  $p$  was kept low. Finally, a validation test composed of five repetitions was executed for each best practice parameter combination identified on glass and carbon-fibre-based

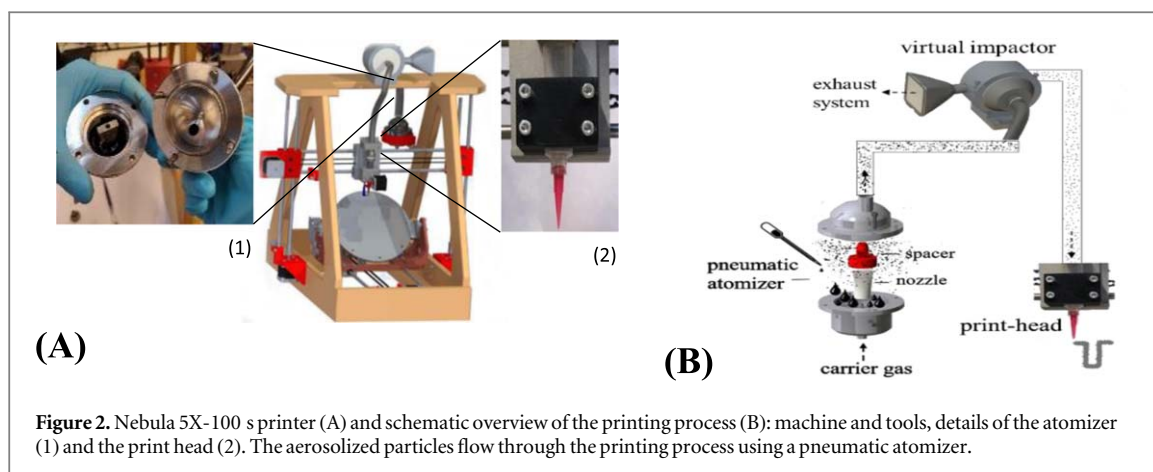


**Figure 2.** Nebula 5X-100 s printer (A) and schematic overview of the printing process (B): machine and tools, details of the atomizer (1) and the print head (2). The aerosolized particles flow through the printing process using a pneumatic atomizer.

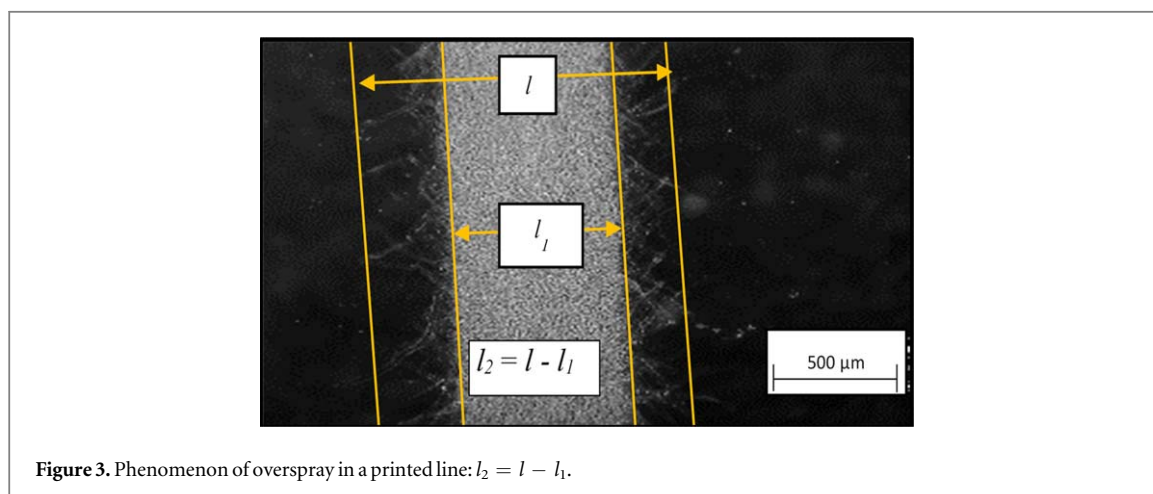


**Figure 3.** Phenomenon of overspray in a printed line:  $l_2 = l - l_1$ .

**Table 3.** Parameter setting for investigation of the printing process on glass, PAN and PAN + CNT substrates under ambient conditions (23 °C, 50% relative humidity).

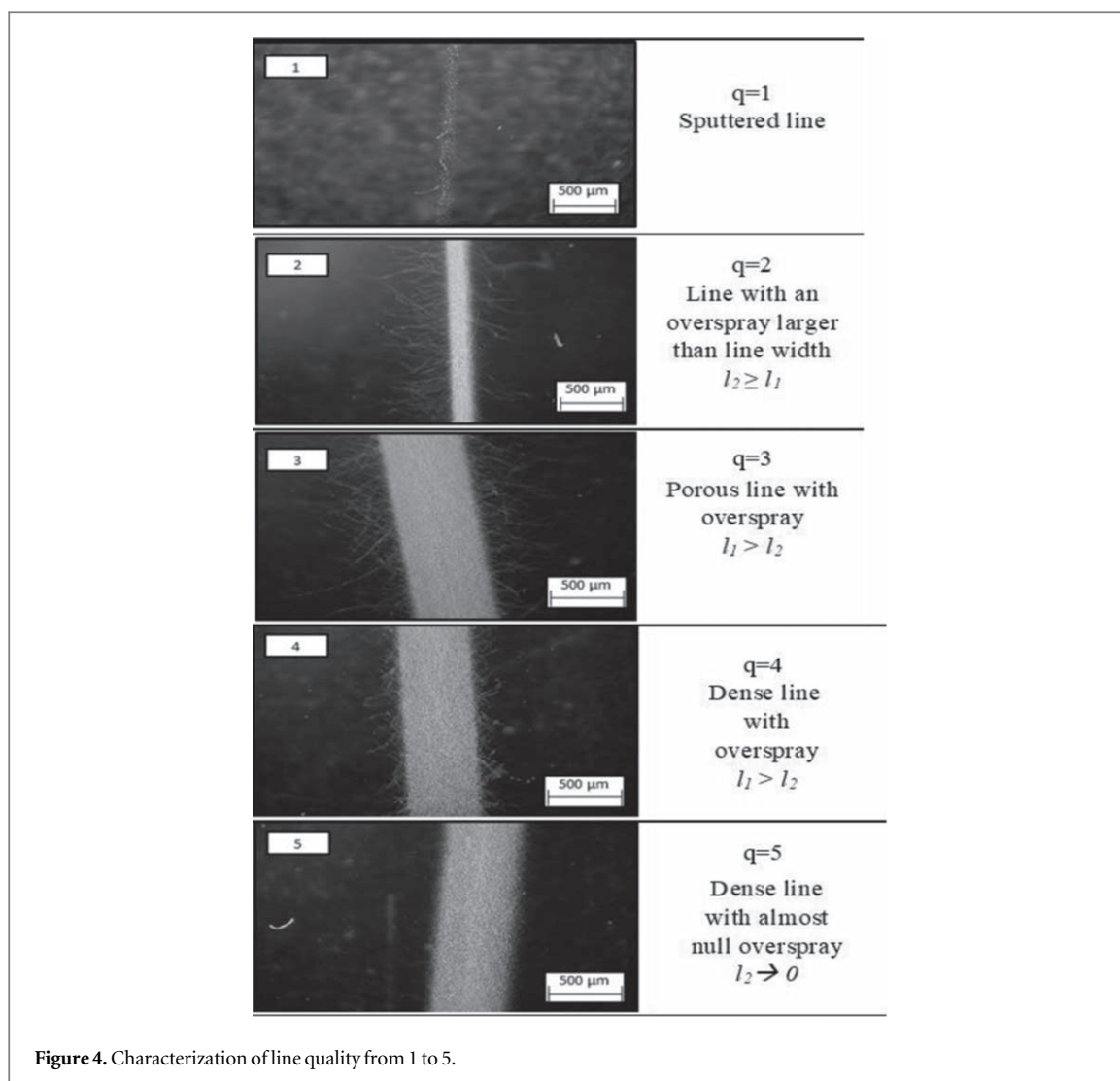
Parameter	Full factorial design screening $2^k$ ( $k > 0$ )		Greedy algorithm investigation			
	Glass substrate		Glass substrate		PAN, PAN + CNT substrates	
Nozzle diameter, $\varnothing$ ( $\mu\text{m}$ )	250	610	250	610	250	610
Stand-off distance, $z$ (mm)	0.7–2	0.8–2.5	$1 \leq z \leq 5^a$	$0.5 \leq z \leq 2^a$	$1 \leq z \leq 3^a$	1.5–1.75
Control pressure, $p$ (bar)	1–2.5	1–2.5	$1 \leq p \leq 2^a$	$1 \leq p \leq 1.75^a$	$1.25 \leq p \leq 2^a$	1.25–1.50
Printing speed, $s$ ( $\text{mm min}^{-1}$ )	50–150	50–150	50	$50 \leq s \leq 150$	30–50–100	50
No. of layers	5–10	5–10	10	10	40	40
Ink			SI-AJ20X			

<sup>a</sup> With an increase of 0.25 for each value tested.

substrates. The samples were in the form of printed lines 10 mm long. After printing, thermal curing (180 °C for 1 h in a Heraeus oven) was applied in order to reach the desired conductivity, due to evaporation of the ink solvent and sintering of the AgNPs. Table 3 lists the experimental conditions selected for each test campaign.

The quality of the printed line,  $q$ , was chosen as the response of interest. In PE, a well-defined track is required to ensure proper electrical transmission, more specifically depending on line density, straightness of

the edge line and the amount of overspray (OS). The OS is here defined as the scattered material deposited, in the form of drops or streams, next to the line edges. For quantification purposes, we chose as the explicit value of the OS ( $l_2$ ), the difference between the line width ( $l$ ) and the line width including the OS ( $l_1$ ) (figure 3). Characterization was conducted by optical microscopy (Hirox KH – 8700). The printed lines were finally ranked from 1 (worst) to 5 (ideal), according to the guidelines given in figure 4, and the parameter combinations leading to  $q \geq 4$  were further validated and



repeated (five times). The electrical resistance  $R$  ( $\Omega$ ) of the best printed samples was also recorded, using a two-point probe method with a Digital Voltmeter 3456 A (HP) on a printed pattern of  $10 \text{ mm} \times 0.3 \text{ mm}$ .

## 2.4. Biocompatibility and cellular adhesion

In the following paragraphs, cell viability assays on human fibroblasts (HFs) and human-induced pluripotent stem cell (iPSC)-derived neural stem cells (NSCs) at different time points are described.

### 2.4.1. Cell viability assay on HFs up to 48 h

Cell culture tests were performed to evaluate the effects of the AgNP ( $\Phi_{\text{avg,particle size}} \sim 100 \text{ nm}$ ) ink SI-AJ20X ink, PAN + CNT mats and printed silver on the fibrous network (PAN + CNTs + Ag) on cellular viability and proliferation. In particular, biocompatibility was first verified on HFs (BJ cell line ATCC<sup>®</sup> CRL-2522<sup>™</sup>) at a single time point of 48 h.

**SI-AJ20X ink.** Three samples of silver SI-AJ20X ink (pure ink, not aerosolized) were painted on glass coverslips and subjected to post-processing thermal curing ( $180^\circ$  for 1 h in a Heraeus oven). Before cell seeding (24-well plate) all the samples were washed

with three times with phosphate-buffered saline (PBS) and sterilized in an autoclave.

**PAN + CNTs.** Three rectangular samples of PAN + CNTs ( $5 \text{ mm} \times 10 \text{ mm}$ ) were washed with PBS for 3 h and sterilized in an autoclave. Subsequently, all samples were placed directly into a 48-well plate.

**PAN + CNTs + Ag.** Six rectangular samples of PAN + CNTs ( $5 \text{ mm} \times 5 \text{ mm}$ ) with 10 printed silver lines were analysed at each point. The printing parameters were as in table 5 for PAN + CNT samples ( $\Phi_{\text{nozzle}} = 610 \mu\text{m}$ ,  $s = 50 \text{ mm min}^{-1}$ ,  $z = 1.5 \text{ mm}$ ,  $p = 1.25 \text{ bar}$ ). Specifically, three samples were printed at  $n = 40$  layers and three at  $n = 1$  layer to highlight the effect of the quantity of printed silver ( $\Phi_{\text{avg,particle size}} \sim 100 \text{ nm}$ ) on cell viability, as mentioned in the literature [51, 54–61]. The samples were subjected to the same post-sintering process as for SI-AJ20X ink ( $180^\circ$  for 1 h in a Heraeus oven), although a different ink–substrate wettability has to be considered. All samples were washed with PBS for 3 h and sterilized in an autoclave before cell culture. Subsequently, all samples were placed directly into a 48-well plate.

**Cell viability assay.** HF were cultured in Dulbecco's modified Eagle's medium (DMEM) with 10% fetal bovine serum, 1% L-glutamine and 1% penicillin/streptomycin (all Euroclone). Cells were maintained at 37 °C in a saturated humidity atmosphere containing 5% CO<sub>2</sub>. A concentrated cell suspension of  $2 \times 10^5$  cells cm<sup>-2</sup> was deposited onto each support and incubated for 30 min before the plate was filled with a suitable volume of DMEM. The biocompatibility was estimated after 48 h by measurement of ATP, using the CellTiter-Glo 3D Cell Viability Assay (Promega cat. no. G9681). This assay is a homogeneous method to detect the number of viable cells based on quantification of ATP, which is a marker for the presence of metabolically active cells. Cells were lysed directly on the substrates according to the manufacturer's instructions. An ATP standard curve (range of 10 μM to 10 nM) was generated using the ATP disodium salt (Promega cat. no. P1132) in order to compare luminescence of samples with luminescence of a standard determining the ATP concentration detected. Luminescence was measured using a Tecan Infinite® M200 multi-functional microplate reader.

#### 2.4.2. Cell viability assay for HF and human-iPSC-derived NSCs up to 96 h

According to the results of the first study on HF at 48 h (see section 3.5), further ATP studies were performed with HF and human-iPSC-derived NSCs on the final product on 24-well plates. The final product is PAN + CNT substrates with 10 printed silver lines at  $n = 40$  layers and the relative printing parameters reported in table 5 ( $\varnothing_{\text{nozzle}} = 610 \mu\text{m}$ ,  $s = 50 \text{ mm min}^{-1}$ ,  $z = 1.5 \text{ mm}$ ,  $p = 1.25 \text{ bar}$ ), subsequently sintered at 180° for 1 h in a Heraeus oven. All samples were washed with PBS for 3 h and sterilized in an autoclave before the cells were cultured. Biocompatibility was estimated after 24, 48 and 96 h (three samples for each point), by measurement of ATP using the same CellTiter-Glo 3D Cell Viability Assay (Promega cat. no. G9681) as described in the previous subsection.

A parallel experiment on ATP measurement with the same Promega assay kit was performed on human-iPSC-derived NSCs and the final product after 24, 48 and 96 h (two samples for each point). Human-iPSC lines reprogrammed and characterized in our laboratory were differentiated into NSCs, using the protocol reported by Ferraro *et al* [65]. Specifically, a Matrigel coating was applied to the substrates for 1 h at 37 °C before cell seeding. A concentrated cell suspension ( $2 \times 10^5$  cells cm<sup>-2</sup>) was deposited onto each sample and incubated for 20 min before filling with an appropriate volume of Neural Expansion Medium.

#### 2.4.3. Immunofluorescence assay

In addition to the quantitative analyses, immunofluorescence assays were performed to observe the cellular

morphology (nuclei and cytoskeleton). Based on previous results, tests were implemented on AgNP ( $\varnothing_{\text{avg,particle size}} \sim 100 \text{ nm}$ ) SI-AJ20X ink and PAN + CNT substrates up to 5 days.

#### 2.4.4. Silver SI-AJ20X ink

Immunofluorescence was performed to study the effects of silver SI-AJ20X ink on glass with respect to cellular adhesion and morphology. Specifically, three samples of silver SI-AJ20X ink were painted on glass coverslips and subjected to post-processing thermal curing (180 °C for 1 h in a Heraeus oven) to evaporate the solvent. All the specimens were washed with PBS three times and sterilized in an autoclave before cell seeding. A concentrated HF cell suspension (BJ cell line ATCC® CRL-2522™) at  $5 \times 10^4$  cells cm<sup>-2</sup> was deposited onto each support and incubated for 30 min before filling the plate with a suitable volume of DMEM. After 5 days in culture, cells were fixed using the Fix&Perm Sample Kit® (SIC) for 30 min (15 min fixation and 15 min permeabilization), incubated with blocking solution (iBind™ 5X Buffer, Invitrogen) for 45 min, and stained with Phalloidin (Sigma Aldrich), which marks the cytoskeletal components of cells. Cell nuclei were then counterstained with Hoechst 33342 for 5 min to highlight the cellular nuclei of living cells. The samples were mounted onto glass slides and observed under an inverted fluorescence microscope (Olympus IX70 inverted microscope); the images were analysed with Image-Pro Plus software v.7.0 (Media Cybernetics).

#### 2.4.5. Adhesion of NSCs on the carbonized substrates

Human-iPSC-derived NSCs [65, 66] were used to perform cell compatibility tests on three samples of PAN + CNT carbonized fibres. The substrates were positioned in a 24-well plate then washed with PBS and sterilized in an autoclave. A Matrigel (Thermo-Fisher Scientific) coating was applied for 1 h at 37 °C. NSCs were passed through a 100 μm strainer (Fisher Scientific) to obtain a single cell suspension and plated at  $5 \times 10^4$  cells cm<sup>-2</sup>. A concentrated cell suspension was deposited on the samples and incubated for 20 min before filling the 24-well plate with the appropriate volume of StemPro NSC SFM (Thermo-Fisher Scientific). Cells were maintained at 37 °C in an atmosphere containing 5% CO<sub>2</sub>. After 5 days in culture, the cells were fixed and permeabilized using Fix&Perm-Reagent kit (SIC), blocked for 45 min with iBind™ Buffer solution (Invitrogen) and stained with Phalloidin, specific for the cytoskeletal component of the cells. Cell nuclei were counterstained with Hoechst 33342 to show the living cells. Samples were observed with an inverted fluorescence microscope (Olympus IX70).

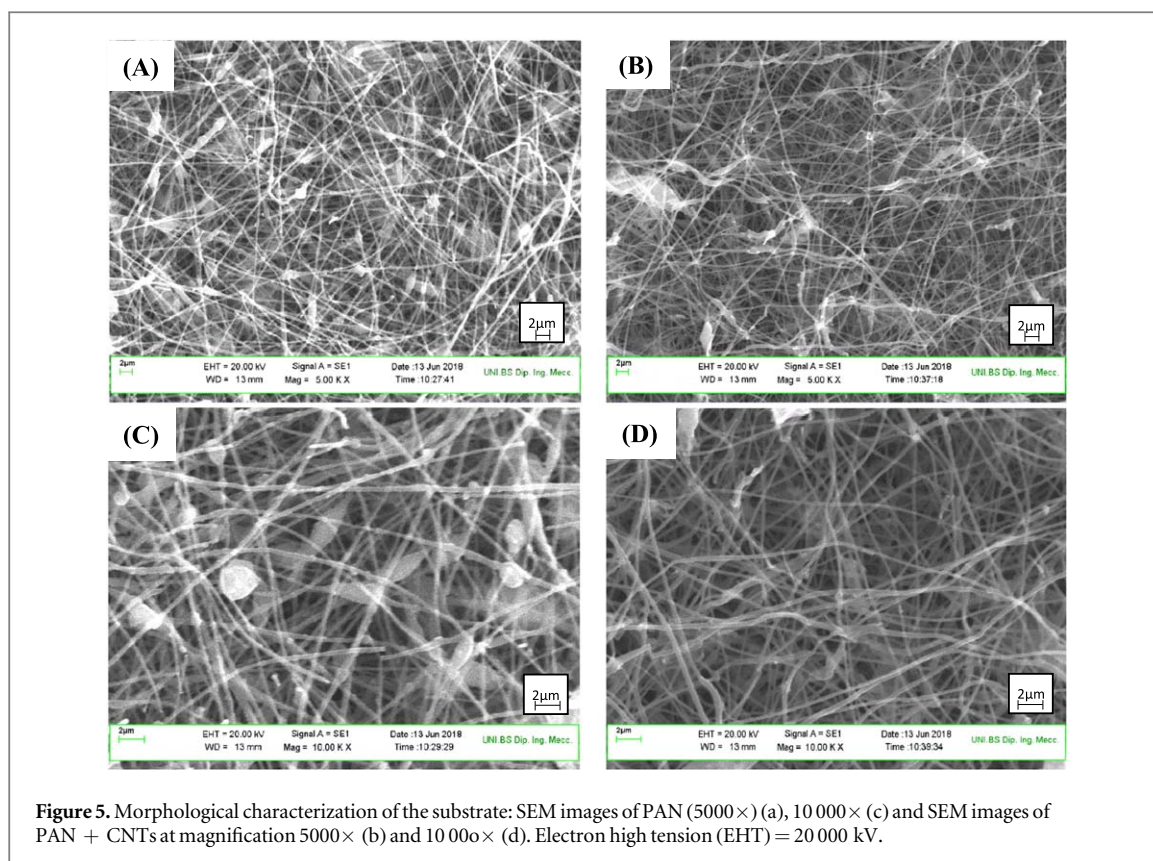


**Figure 5.** Morphological characterization of the substrate: SEM images of PAN (5000 $\times$ ) (a), 10 000 $\times$  (c) and SEM images of PAN + CNTs at magnification 5000 $\times$  (b) and 10 000 $\times$  (d). Electron high tension (EHT) = 20 000 kV.

### 3. Results and discussion

#### 3.1. Substrate characterization

Morphological characterization of PAN and PAN + CNTs (diameter of fibres, density of the fibrous networks, orientation of fibres and presence of beads in the pattern) was carried out. Figure 5 shows SEM images for both PAN and PAN + CNTs at two levels of magnification. Both the substrates present an homogeneous distribution of randomly oriented fibres.

PAN samples have a higher density of fibres than PAN + CNTs. PAN fibres seem more tangled and with a higher concentration of round beads. The formation of some beads might be related to poor dispersion of the nanoparticles and incomplete solvent evaporation: this suggests that, although CNTs seemed to be well dispersed by sonication in DMF, some of the long nanotubes were entangled with each other. Further electrospinning parameter optimization will be performed to avoid these defects. The average thickness of the PAN + CNT material is 190  $\mu\text{m}$  ( $\sigma^2 = 0.02$ ), compared with the 310  $\mu\text{m}$  ( $\sigma^2 = 0.06$ ) for PAN. The TEM images exhibit the differences in the fibre surfaces (figure 6): the PAN + CNT fibres have a multi-layered wall of CNTs in the shell region (figure 6(a)). A distinction between core and shell regions is detected close to the fibre surface. Here it is possible to distinguish the orientation of the fringe in the shell region, which indicates good alignment of the CNTs along the fibre axis. A higher

grade of graphitization in PAN + CNT than in PAN fibres is also detected (figure 6(b)): the electron diffraction pattern shows concentric circles formed from multiple sets of six-fold symmetrical spots, which are an index of the grade of graphitization in the fibrous network. This derives from the multi-layered distribution of  $\text{sp}_2$  hybridized carbon planes (from CNTs and/or grown carbon crystals) which are randomly oriented with respect to the incident electron beam.

Measurement of the resistivity  $\rho$  shows that PAN and PAN + CNTs are slightly conductive in the same range of  $\sim 2 \Omega \text{ cm}$ . This result can be interpreted from a morphological point of view: even if the embedded CNTs have increased the conductivity of the fibres, their less ordered orientation decreased the propagation of electrical current in the matrix. Table 4 reports a summary of the material properties which have been characterized.

#### 3.2. Ink–substrate interaction

High wettability of silver ink is revealed for all the samples, showing good interaction between the ink and the substrates. This phenomenon usually favours a high quality of printed lines for a given best practice printing approach. Figure 7 reports the contact angle measurements on each substrate. Specifically, both PAN and PAN + CNTs reveal the highest wettability, most likely due to their mat structure, and consequently higher absorption.

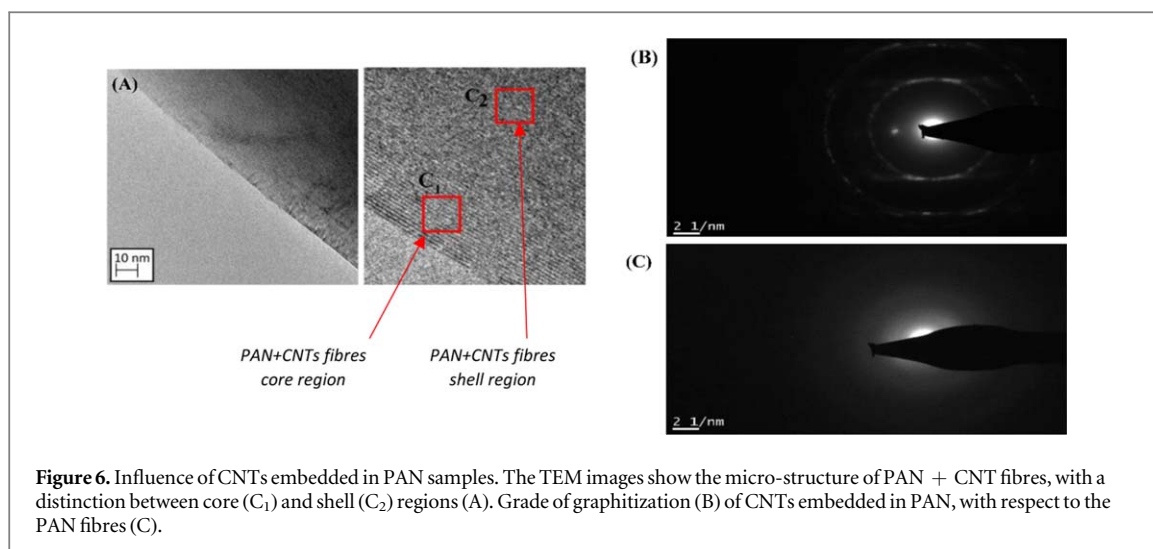


**Figure 6.** Influence of CNTs embedded in PAN samples. The TEM images show the micro-structure of PAN + CNT fibres, with a distinction between core (C<sub>1</sub>) and shell (C<sub>2</sub>) regions (A). Grade of graphitization (B) of CNTs embedded in PAN, with respect to the PAN fibres (C).

**Table 4.** Material characterization. The table reports the values of morphological and electrical characterizations, respectively, for PAN and PAN + CNT materials.

Material property	Mean ( $\mu$ ) or standard deviation ( $\sigma^2$ )	PAN	PAN + CNT
Fibre diameter, $d$ ( $\mu\text{m}$ )	$\mu$	0.29	0.27
	$\sigma^2$	0.05	0.05
Substrate thickness, $t$ (mm)	$\mu$	0.31	0.19
	$\sigma^2$	0.06	0.02
Sheet resistance, $\sigma$ ( $\Omega \square^{-1}$ or $\Omega$ )	$\mu$	67.1	102.6
	$\sigma^2$	9.5	21.3
Resistivity, $\rho$ ( $\Omega \text{ cm}$ )	$\mu$	2.1	1.9
Crystallite thickness, $L$ (nm)	$\mu$	—	15.1
	$\sigma^2$	—	4.9

### 3.3. Printing experiment

#### 3.3.1. Glass substrate and silver ink

Figure 8 shows the analyses of the results obtained on glass for a full factorial screening design on both nozzles.

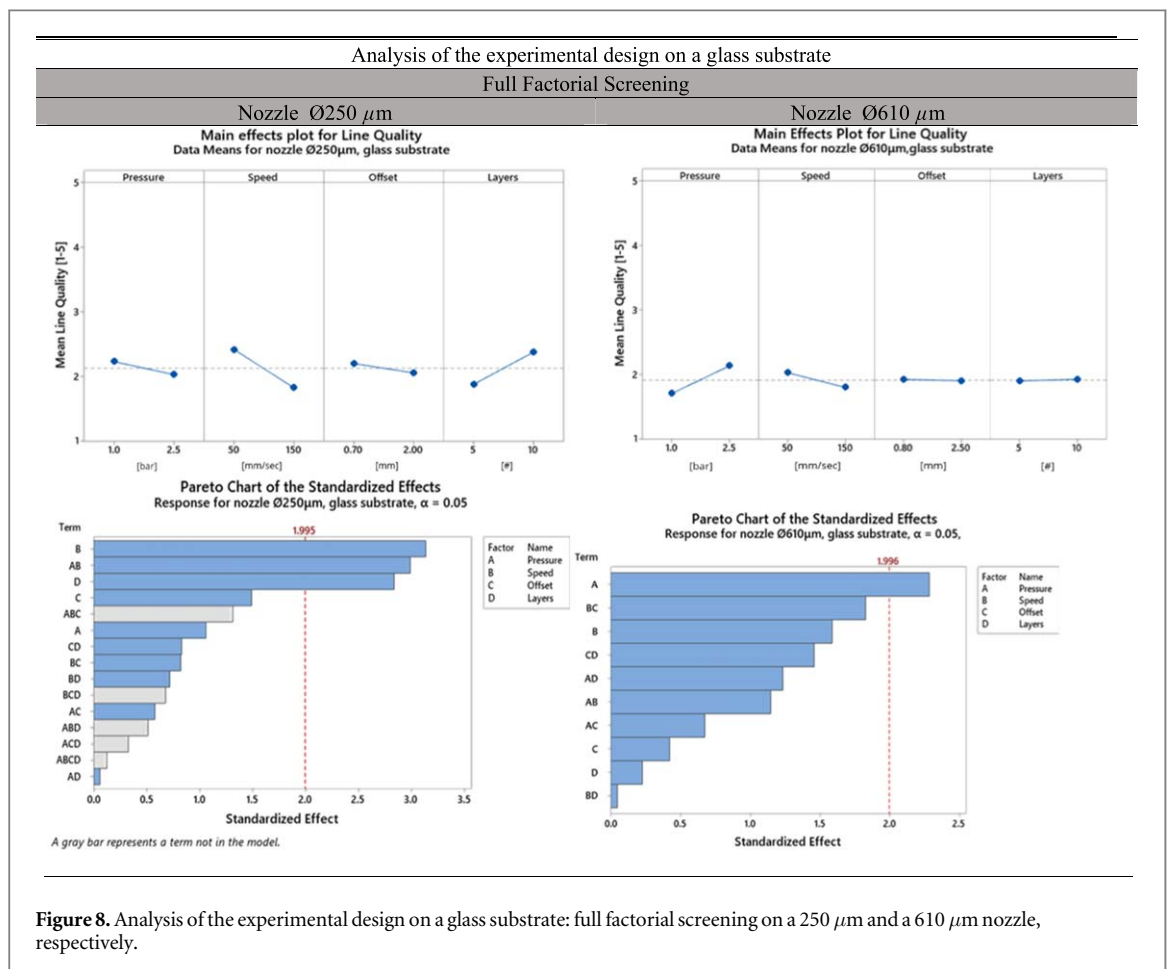
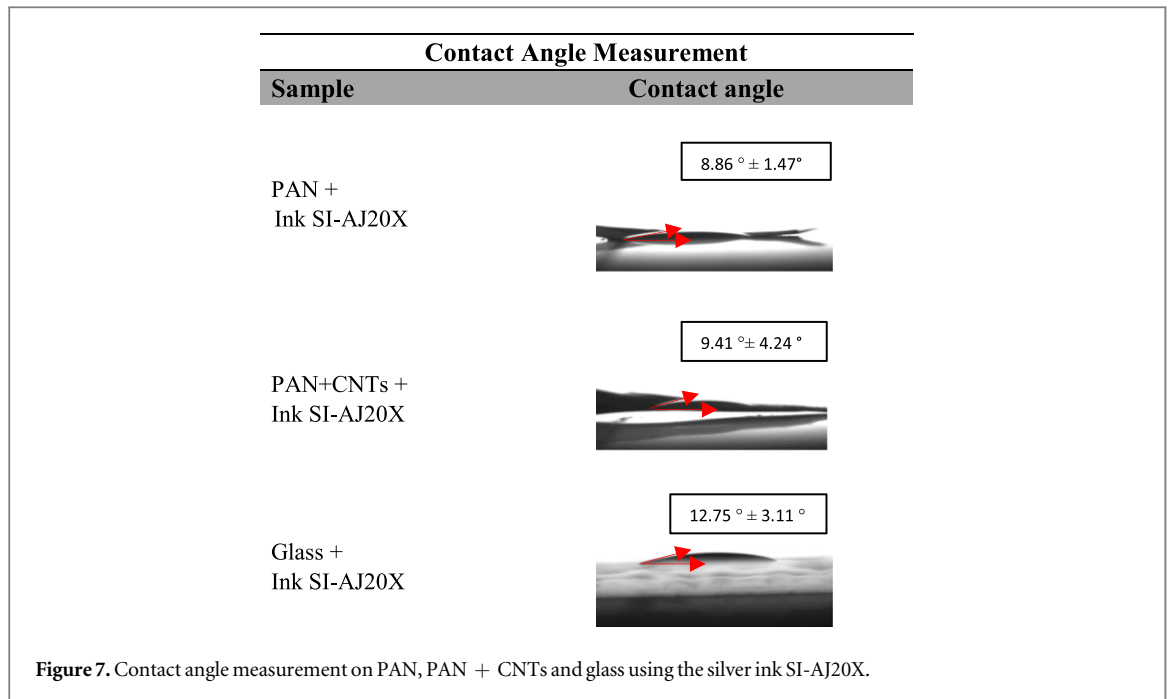
With the use of a 250  $\mu\text{m}$  nozzle (figure 8, Pareto Chart), the most significant parameters are, in order: the printing speed,  $s$ , the interaction between the control pressure and printing speed,  $ps$ , and the number of layers,  $n$ . In addition, the main effect plot shows a small increase in line quality when  $s$  assumes low values and the number of deposited layers,  $n$ , increases, this latter being directly proportional to the line density. Instead, the pressure,  $p$ , is revealed to be the most significant parameter when using a 610  $\mu\text{m}$  nozzle. The effect of pressure is also opposite when comparing the results obtained with the two nozzle diameters. This effect can be explained by referring to Bernoulli's principle, according to which the kinematic status of a fluid is inversely proportional to the cross-sectional area of the vessel through which the fluid is flowing.

On average, the results are assessed as being of quality 2, with small variations with changes of the input parameters (figure 8, Main Effects). The

regression analyses for a 250  $\mu\text{m}$  and a 610  $\mu\text{m}$  nozzle give, respectively,  $R_{250\mu\text{m}}^2$  32.10% and  $R_{610\mu\text{m}}^2$  26.21%, hence indicating that, in the selected window, the investigated parameters are only partially responsible for the results obtained.

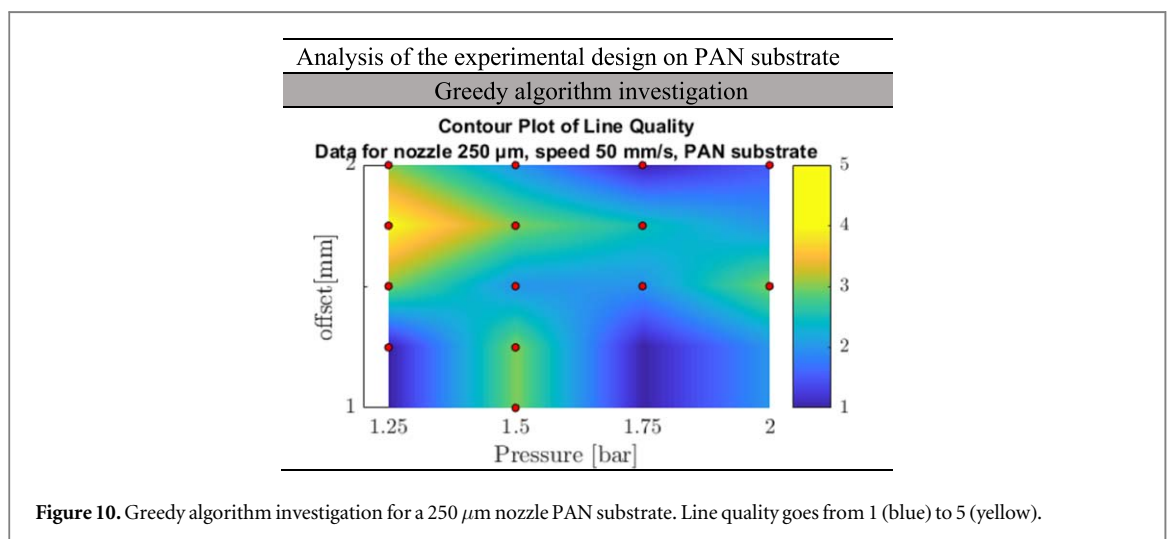
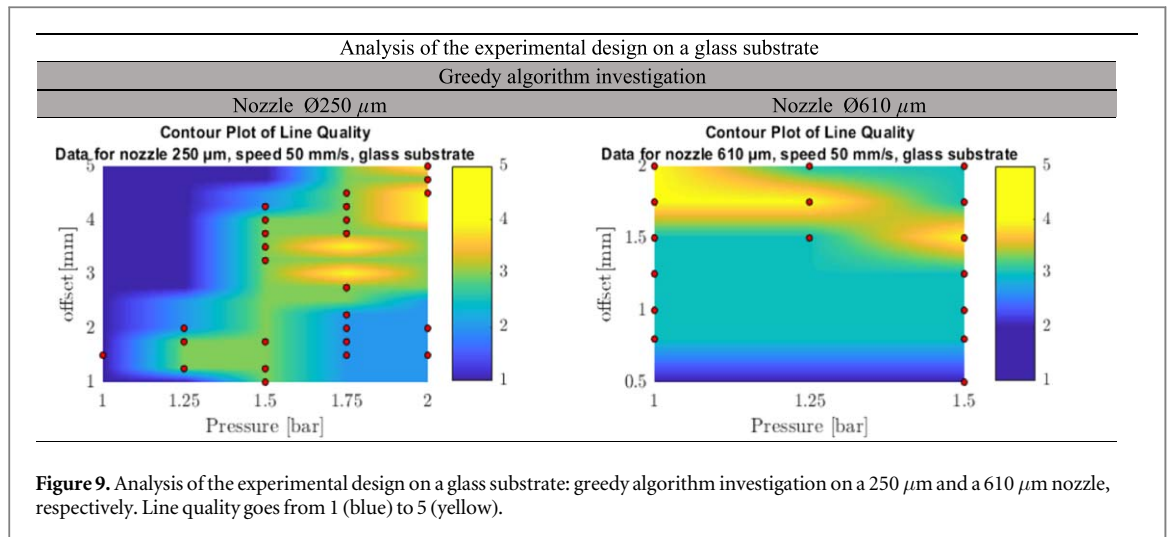
Accordingly, a greedy algorithm was performed in an adapted process window for further parameter investigation. The experimental campaign was specifically applied on  $p$  and  $z$  (off-set distance, introduced based on the previous experience acquired), by gradually increasing the parameter values, one by one, and by performing the printable combinations only. The  $p$  values were intentionally kept on the lower side to ensure more robust results. Figure 9 shows the contour plot for the line quality with variation of off-set and pressure. The graph is the result of experimental data obtained for given combinations of  $p$  and  $z$  and interpolated data when not present.

Non-linear behaviours could also be detected, as intervals of four or more levels were investigated. The quality results are promising (up to level four), but they are still fluctuating without revealing a particular trend. The contour plot does not reveal the presence of a global optimum, but only local best parameter combinations.



In general,  $q \geq 4$  can only be obtained at low  $p$  and  $z$ ; instead, if  $z$  is higher than 0.75 mm, the desired quality  $q \geq 4$  can be achieved with increasing  $p$  for a 250 μm nozzle. For this reason, the best practice is chosen as:  $s = 50 \text{ mm min}^{-1}$ ,  $z = 3.5 \text{ mm}$ ,  $p = 1.75 \text{ bar}$

and  $n = 10$  layers. Instead, a  $q \geq 4$  can be achieved with low  $s$  and  $p$  and high  $z$ , or vice versa, for a 610 μm nozzle. For this reason, the best practice is:  $s = 50 \text{ mm min}^{-1}$ ,  $z = 1.75 \text{ mm}$ ,  $p = 1.25 \text{ bar}$  and  $n = 10$  layers. Those combinations of parameters will



eventually be repeated and further validated, as reported in section 3.4.

### 3.3.2. PAN, PAN + CNT substrates and silver ink

According to the analysis developed on glass substrate, a similar greedy algorithm investigation was applied to PAN and PAN + CNT substrates. The experimental analysis started with a 250  $\mu\text{m}$  nozzle and focused on  $p$  and  $z$ , by gradually increasing the parameter values of 0.25, one by one, and performing printable combinations only. Figure 10 shows the contour plot for the line quality obtained for given combinations of  $p$  and  $z$ , with the use of a 250  $\mu\text{m}$  nozzle on PAN substrate. As for glass substrate, interpolation of the experimental data shows non-linear behaviour. The same range of quality line (up to level four) is detected with local best parameter combinations but without a specific trend. In general,  $q \geq 4$  can only be obtained at low  $p$  and  $z$ ; for this reason, the best practice is chosen as:  $s = 50\ \text{mm}\ \text{min}^{-1}$ ,  $z = 1.75\ \text{mm}$ ,  $p = 1.25\ \text{bar}$  and  $n = 40$  layers. A more restricted parameter window was studied for a 610  $\mu\text{m}$  nozzle. The experiments were based on the previous results on PAN and PAN + CNT substrates using a 250  $\mu\text{m}$

nozzle and on the analyses performed on glass substrate using a 610  $\mu\text{m}$  nozzle. With this knowledge,  $q \geq 4$  is detected to be obtained again at low  $p$  and  $z$ ; the best practice is chosen as:  $s = 50\ \text{mm}\ \text{min}^{-1}$ ,  $z = 1.5\ \text{mm}$ ,  $p = 1.25\ \text{bar}$  and  $n = 40$  layers.

### 3.4. Validation test and best printing practices

Table 5 reports the best printing combinations obtained for glass, PAN and PAN + CNT substrates, respectively. Five repetitions for each combination of parameters were conducted to validate the results. The results were characterized with regard to line width, OS and achieved electrical resistance. The quality of the results was also cross-checked and confirmed to have a value of at least 4, as in previous experiments. No difference was detected in the best practice values for both the nozzles on PAN and PAN + CNT substrates because the two fibrous networks can be considered as a similar substrate from the point of view of the printing process. Specifically, a comparison between the carbon-fibre substrates and the glass substrate reveals that, for a 250  $\mu\text{m}$  nozzle, a lower pressure is required, which needs consequently a lower

**Table 5.** Best practice printing parameters for glass, PAN and PAN + CNT substrates using silver ink SI-AJ20X, with the respective results (margin of error with confidence level of 95%).

Inputs	Glass substrate	PAN	PAN + CNTs			
$\emptyset$ ( $\mu\text{m}$ )	250	610	250	610	250	610
$z$ (mm)	3.5	1.75	1.75	1.5	1.75	1.5
$p$ (bar)	1.75	1.25	1.25	1.25	1.25	1.25
$s$ ( $\text{mm min}^{-1}$ )		50			50	
$n$		10			40	
			Output			
Line width, $l_1$ ( $\mu\text{m}$ )	$392.9 \pm 12.2$	$592.4 \pm 47.1$	$74.1 \pm 7.9$	$386.9 \pm 33.9$	$84. \pm 11.1$	$391.7 \pm 45.6$
Overspray, $l_2$ ( $\mu\text{m}$ )	$134.7 \pm 13.9$	$196.9 \pm 23.6$	$19.4 \pm 3.6$	$27.1 \pm 31.3$	$28.9 \pm 8.4$	$68.1 \pm 19.9$
Electrical resistance, $R$ ( $\Omega$ )	$53.4 \pm 2.2$	$43.7 \pm 0.7$	$54.1 \pm 5.5$	$61.5 \pm 0.6$	$127.6 \pm 14.$	$135.5 \pm 28.5$
Quality (1–5)			4			

stand-off distance (according to the Bernoulli principle). This is because of the high fragility of the substrates. On the other hand, the use of a 610  $\mu\text{m}$  nozzle requires for each substrate a low pressure equal to  $p = 1.25$  bar. In this case, instead, the main difference between glass and carbon-fibre-based substrates is found in the off-set  $z$ : a lower  $z$  is set for PAN and PAN + CNT substrates, due to the absorption of aerosolized micro-droplets inside the fibrous mats. As a consequence, a higher number of printed layers ( $n = 40$ ), than that on glass ( $n = 10$ ), is also required. This condition also explains the smaller values of line width and OS with respect to the results obtained on glass.

The overall analysis demonstrates the feasibility of printing conductive lines on electrospun fibrous patterns. The values of electrical resistance on glass and PAN substrates are approximately in the range of 50  $\Omega$ , which is in line with the PE requirements. Instead, PAN + CNT substrates exhibit higher electrical resistance, due to the higher sheet resistance (see table 4), which induces more significant signal dispersion. Hence, the morphology and conductivity of the substrate influence the creation of efficient bio-electrical systems. In addition, the results regarding line width values are in line with their respective  $\emptyset_{\text{nozzle}}$  size, even if parameter optimization based on the relative stand-off distance can be performed. Specifically, although the micro-scale resolution of the line width in terms of system performance cannot reach that of industrial nebulized jet-based printers, such as the Aerosol Jet<sup>®</sup> printers by Optomec (down to 10  $\mu\text{m}$ ) [39] or Nanojet<sup>™</sup> (NJ) printers by IDS (down to 15  $\mu\text{m}$ ) [67], it is comparable from the point of view of cost-effectiveness. This can open up possibilities in a low-cost market scenario.

### 3.5. Biocompatibility and cellular adhesion

Figure 11 reports ATP assay results (time point 48 h) of HFs cultured on SI-20X ink droplets, PAN + CNT samples and their combination, respectively. The relative values of %ATP concentration of samples,

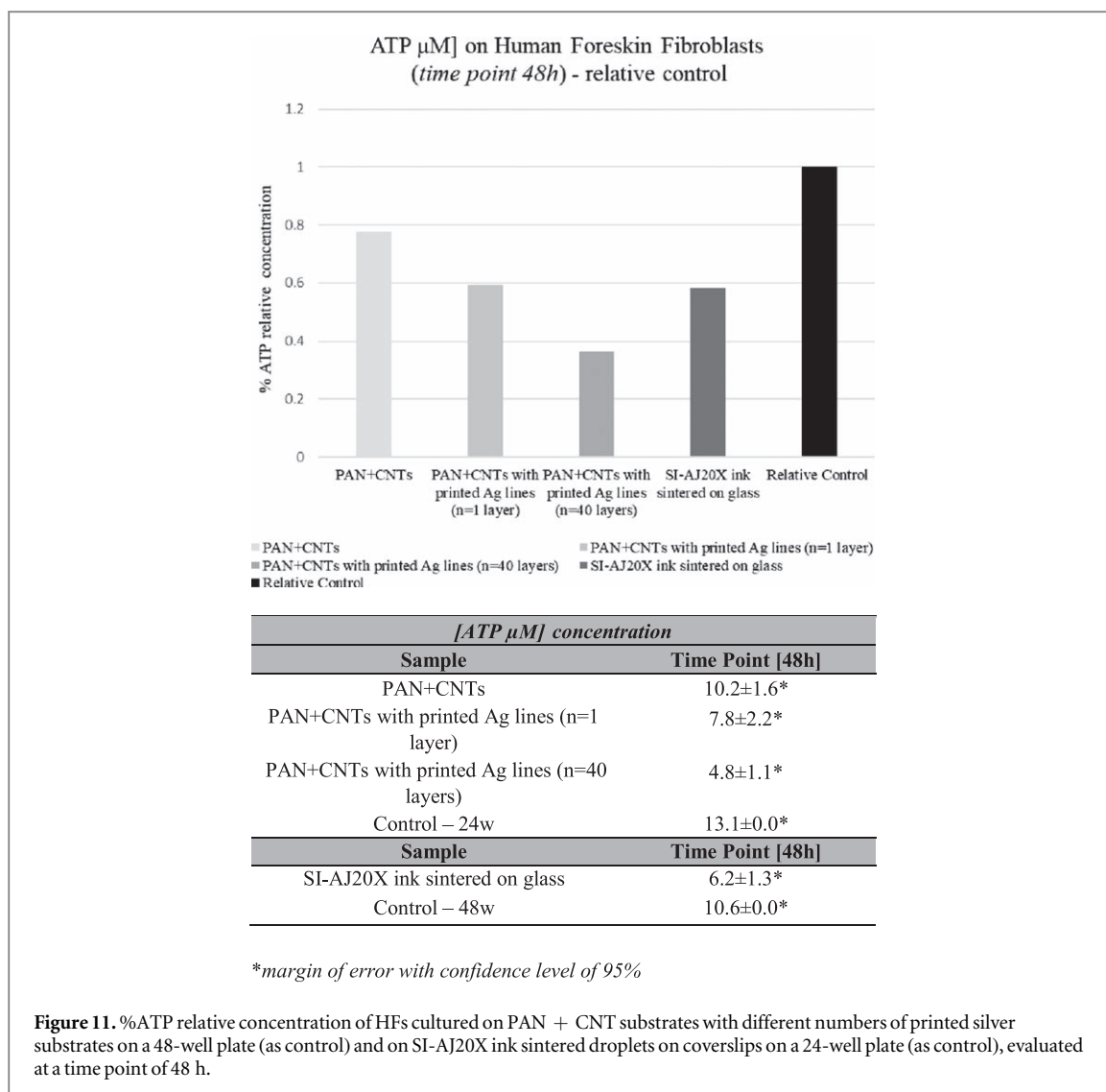
with respect to the corresponding control sample, are shown in the graph, while ATP ( $\mu\text{M}$ ) concentrations are reported in the table. As a first observation, PAN + CNT mats reveals the highest biocompatibility, while PAN + CNTs + Ag at  $n = 40$  layers has the lowest value. PAN + CNTs + Ag at  $n = 1$  layer and silver ink painted on glass coverslips have intermediate values.

Specifically, despite the presence of CNTs in the fibrous network, PAN + CNT substrates are sufficiently biocompatible with respect to the control sample. Besides, the existence of ‘beads’ in the electrospun fibres, produced by incomplete evaporation of the solvent in the solution, does not seem to have a considerable influence on cell viability and proliferation.

The results on PAN + CNT + Ag samples, with regard to the variation of AgNP suspensions, also reveal the toxicity of silver ink and its dose-dependent nature. This is in accordance with the complex relative nature of the biological activity of AgNP powders, in a multi-factorial dose-, agglomeration- and dissolution rate-dependent environment. In addition, PAN + CNT + Ag samples at  $n = 40$  layers show lower %ATP concentrations than silver ink droplets on glass coverslips. This may be explained by specific surface–cell interactions, caused by the different deposition processes: nebulized jet-based printing and painting, respectively. We observed in our experiments that printed lines delaminate more easily on glass than on the carbon-fibre substrates. Hence, we assume that the nebulized jet-based printing process can cause different AgNP particle agglomerations, resulting in distinctive Ag<sup>+</sup> ion release and cell interaction. This effect will be analysed in future studies.

Figure 12 shows ATP ( $\mu\text{M}$ ) concentrations (time points 24, 48 and 96 h) of HFs and human-iPSC-derived NSCs, cultured on PAN + CNT with printed Ag substrates (10 lines at  $n = 40$  layers). Specifically, HFs proliferation follows a positive growth trend on the final product for the first time points, and a negative one visible at 96 h (figure 12(A)).

The intrinsic variability of the nebulized jet-based process in terms of the quantity of silver deposited on



the substrate (as previous data confirmed) has an influence on the toxicity of the different samples. However, proliferation of human-iPSC-derived NSCs follows a negative trend by 48 h (figure 12(B)), reaching values approximately equal to zero. In this context, it must be noted that the cells used are not primary neurons. These results demonstrate the unfeasibility of direct contact between commercial AgNP ( $\varnothing_{\text{avg,particle size}} \sim 100$  nm) ink commonly used in PE and neural cells.

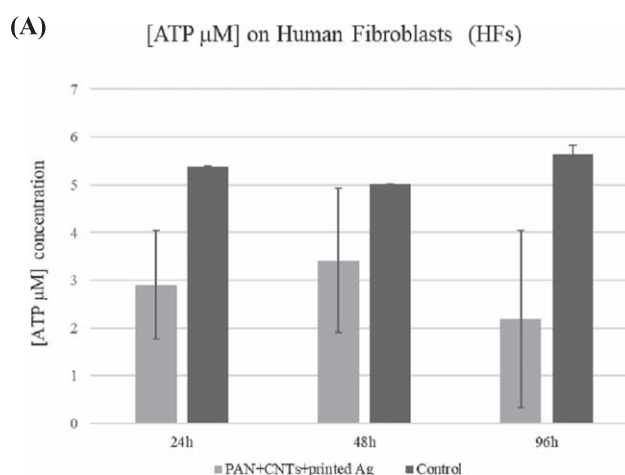
### 3.5.1. Immunofluorescence assay

Figure 13 reports immunofluorescence microscopy images of HF<sub>s</sub> on a drop of SI-AJ20X silver ink and iPSC-derived NSCs on PAN + CNT carbonized fibres in different regions of the substrate, after 5 days. Specifically, the sintered droplets of silver ink can tolerably sustain cell adhesion and survival, even if HF<sub>s</sub> seem to suffer, as confirmed by the staining of nuclei and the cytoskeleton (figure 13, top row). On the other hand, immunofluorescence images of adhesion of iPSC-derived NSCs on PAN + CNTs (figure 13, bottom row) show that cells spread on the

available surface, confirming the recognition of the substrate. Human-iPSC-derived NSCs colonize the fibrous network as the cytoskeletal protrusions are interconnected through the carbon fibres. These promising results lead to the possibility of differentiating the stem cells into neurons on the pyrolysed scaffolds to enhance the maturation of adult cells by the application of morphological, mechanical and electrical stimuli.

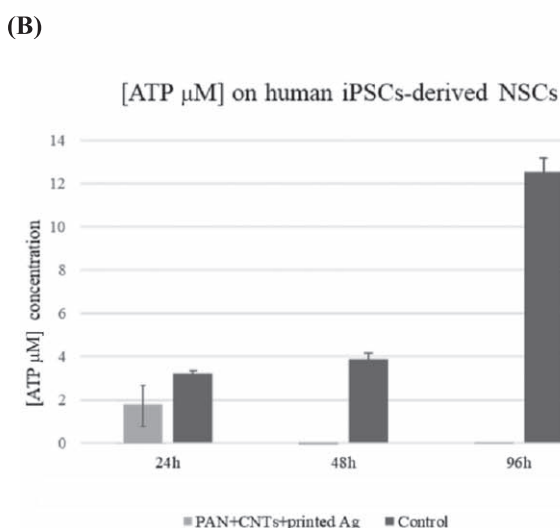
## 4. Application and future activities

A designed RC (resistance—capacitor) circuit for standard printed electronics application, such as LEDs, was printed on glass and PAN + CNT substrates to test the feasibility of printing functional conductive patterns and circuits, as shown in figure 14. On a glass substrate, an electrical resistance of  $\sim 130 \Omega$  was measured across the rectangular pads (connecting printed line width  $l_1 = 606.8 \pm 33.1 \mu\text{m}$ , rectangular area  $\sim 3.4 \text{ mm}^2$ ), indicated as 1 and 2 in figure 14(a). On the same path, values of  $\sim 480 \Omega$  were instead



[ATP $\mu\text{M}$ ] concentration Sample (HFs)	Time Point [h]		
	24h	48h	96h
PAN+CNTs +printed Ag	2.9 ± 1.1*	3.4 ± 1.5*	2.1 ± 1.8*
Control	5.4 ± 0.0*	5.0 ± 0.0*	5.6 ± 0.2*

\*margin of error with confidence level of 95%



[ATP $\mu\text{M}$ ] concentration Sample (iPSCs-derived NSCs)	Time Point [h]		
	24h	48h	96h
PAN+CNTs +printed Ag	1.8 ± 0.9*	0.0	0.0
Control	3.2 ± 0.1*	3.9 ± 0.3*	12.5 ± 0.6*

\*margin of error with confidence level of 95%

**Figure 12.** ATP concentrations ( $\mu\text{M}$ ) of HFs (A) and human-iPSC-derived NSCs (B) cultured on PAN + CNT with printed Ag substrates (10 lines,  $n = 40$  layers) and on a 48-well plate (as control), estimated at different time points (24 h, 48 h, and 96 h).

measured on PAN + CNTs (figures 14(b) and (d)), validating the functionality of the printed circuit also for high sheet resistance bio-conductive mat pads (connecting printed line width  $l_1 = 424.4 \pm 55.3 \mu\text{m}$ , rectangular area  $\sim 3.6 \text{ mm}^2$ ).

These results represent a starting point for future investigations on ES across scaffolds in culture medium, such as the design of circuits with rectangular

biphasic pulse generators and no residual charges [18, 68]. By means of a DC power supply, for instance, ES can be achieved through establishment of an electrical field, uniformly distributed on the external membrane of the cells [69] and with specific voltages in the range of  $4.5\text{--}450 \text{ mV mm}^{-1}$ .

Several methods have already been investigated in the literature in order to overcome the toxicity of

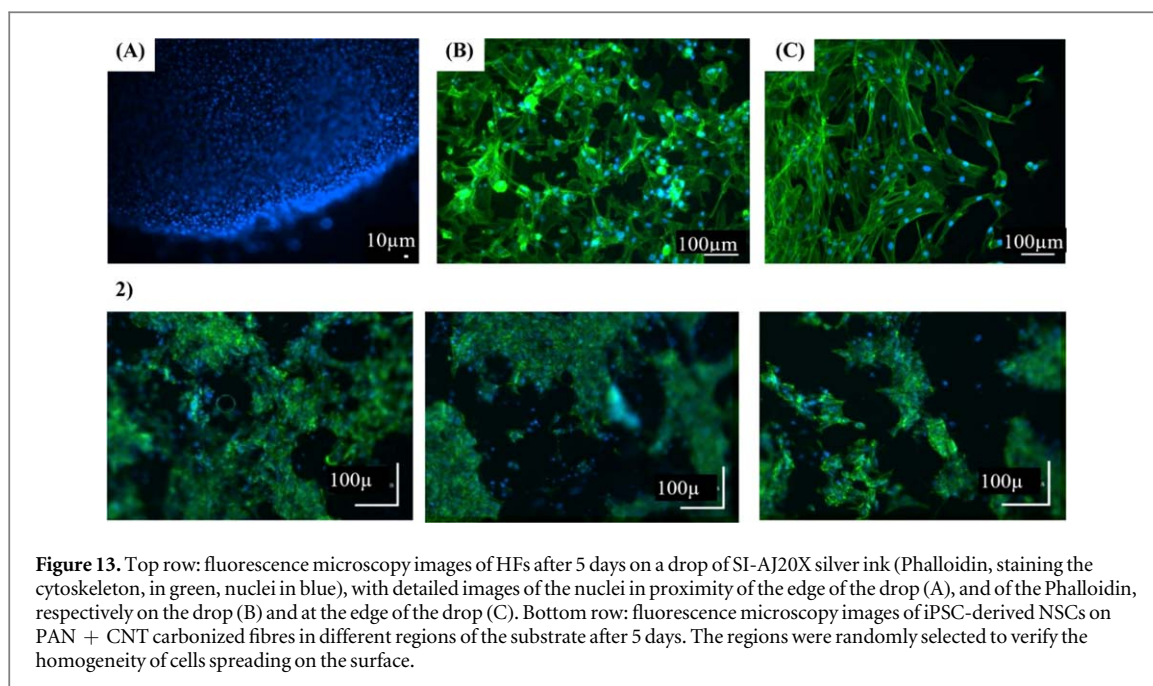


**Figure 13.** Top row: fluorescence microscopy images of HFs after 5 days on a drop of SI-AJ20X silver ink (Phalloidin, staining the cytoskeleton, in green, nuclei in blue), with detailed images of the nuclei in proximity of the edge of the drop (A), and of the Phalloidin, respectively on the drop (B) and at the edge of the drop (C). Bottom row: fluorescence microscopy images of iPSC-derived NSCs on PAN + CNT carbonized fibres in different regions of the substrate after 5 days. The regions were randomly selected to verify the homogeneity of cells spreading on the surface.

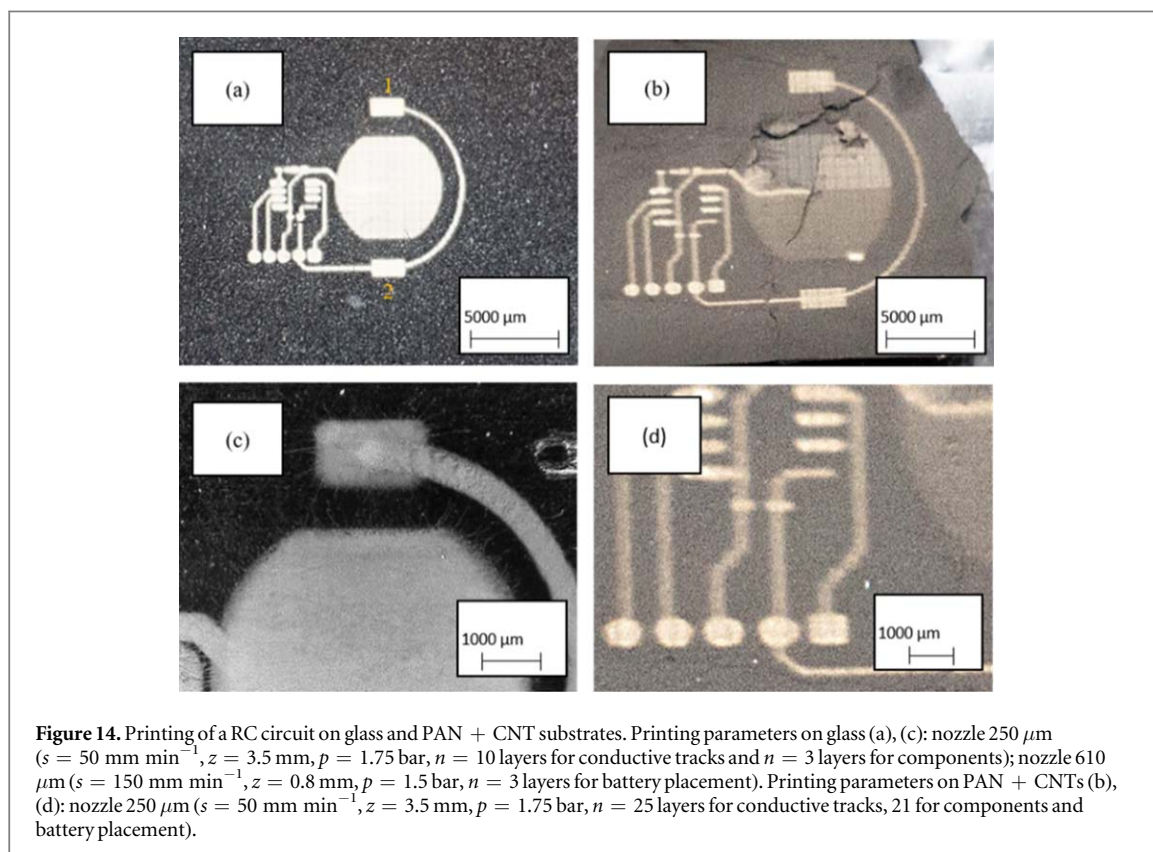


**Figure 14.** Printing of a RC circuit on glass and PAN + CNT substrates. Printing parameters on glass (a), (c): nozzle 250  $\mu\text{m}$  ( $s = 50 \text{ mm min}^{-1}$ ,  $z = 3.5 \text{ mm}$ ,  $p = 1.75 \text{ bar}$ ,  $n = 10$  layers for conductive tracks and  $n = 3$  layers for components); nozzle 610  $\mu\text{m}$  ( $s = 150 \text{ mm min}^{-1}$ ,  $z = 0.8 \text{ mm}$ ,  $p = 1.5 \text{ bar}$ ,  $n = 3$  layers for battery placement). Printing parameters on PAN + CNTs (b), (d): nozzle 250  $\mu\text{m}$  ( $s = 50 \text{ mm min}^{-1}$ ,  $z = 3.5 \text{ mm}$ ,  $p = 1.75 \text{ bar}$ ,  $n = 25$  layers for conductive tracks, 21 for components and battery placement).

AgNP solutions, for example surface coating [70, 71] and silver encapsulation via a printed passivation layer. Specifically, several chemicals can be applied as surface coating agents to avoid direct interaction with the biological system, preventing the oxidation of  $\text{Ag}^+$  ions. Citrate and polyvinylpyrrolidone can be used as surface coating agents for AgNPs [51], but also PDMS, polyimide [23] or parylene-C [71, 72], as passivation and insulating (printed) layers. Therefore, considering that direct contact between the biological system and

AgNP inks designed for printing of electronics is not possible, due to high levels of toxicity, potential encapsulation via a surface coating or a printed layer will be surely investigated in future studies.

## 5. Conclusion

An ideal neural scaffold will usually have multiple cues for axon guidance; these could be obtained by

introducing conductive electrodes [2, 4]. The present study investigates the feasibility of using printing of electronics for bio-electrical neural tissue engineering applications by means of a nebulized jet-based printing process. More specifically, the study has concerned: (i) production of biocompatible electrospun-pyrolysed fibrous mats via the electrospinning of neural cell cultures (PAN, mean fibre diameter  $d = 0.29 \mu\text{m}$ , sheet resistance  $\rho_{\mu} = 67.1 \Omega \square^{-1}$ ), with the addition of embedded CNTs (PAN + CNTs, mean fibre diameter  $d = 0.27 \mu\text{m}$ , sheet resistance  $\rho_{\mu} = 102.6 \Omega \square^{-1}$ ); (ii) identification of the most suitable combination of parameters for printing conductive lines on these substrates; (iii) toxicity tests of the selected substrates and ink; and (iv) printing of a functional circuit for concept validation.

The results showed high wettability for ink-substrate adhesion, allowing the possibility of printing well-defined and functional patterns, without delamination/desquamation in physiological solutions, and with electrical resistances in the range of  $50 \Omega$  for both glass and PAN substrates, and in the range of  $130 \Omega$  for PAN + CNT substrates for a best practice combination of print parameters and sintering processes.

However, the cytotoxic effects of the most common ink used in PE, such as AgNP ( $\phi_{\text{avg,particle size}} \sim 100 \text{ nm}$ ) solutions, on HFs and human-iPSC-derived NSCs via ATP assay for three-dimensional cell cultures, suggest the need to implement surface coating or encapsulation of the circuit in order to increase cell viability. Future studies will focus on this. On the other hand, the work demonstrates the technological potential of applying PE techniques to produce innovative bio-electrical scaffolds for drug discovery or neural ES for *in vitro* models, with enhancements of connection efficiency among cells and substrates. In fact, the main advantage of the nebulized jet-based printing technique is its versatility: both planar and free-formed substrates, flexible or rigid supports, textile and paper, can be investigated, even if its application to biomaterials or biomimetic tissues is still unusual. Based on the literature evidence, examples in the field of tissue engineering [37, 71] have already been demonstrated. Furthermore, the possibility of printing with a broad selection of inks, which can balance biocompatibility and electrical conductivity (such as PEDOT:PSS, collagen, carbon-based inks, etc), can completely avoid the problems concerning potential cytotoxic effects.

Future work will involve optimization of electrospinning parameters and the investigation of printing with biocompatible inks for the design and validation of conductive PE on tissues for neuronal stimulation and related differentiation, but also axon guidance and neurite outgrowth studies. Eventually, further study on the potential production of three-dimensional conductive scaffolds, already on-going on nanofibres [3, 18], will be implemented using nozzle-based printing techniques [33] in a multi-material/multi-functional vision.

## Acknowledgments

We would like to express our gratitude to Dr Fernando Cortes for providing silver ink from Agfa (Belgium) and U Hasselt for giving us the possibility to perform wettability measurements. We also thank the AML Lab for technical support and critical discussions during the experiments, in particular Akash Verma and Jie Zhang. Finally, we would like to thank Mohit Sharma (ESAT, KU Leuven) for fruitful discussions regarding data analyses, and Patrick Pelgrims and Yurre De Weerd (Thomas More, Belgium) for providing the electrical design circuit.

## ORCID iDs

Miriam Seiti  <https://orcid.org/0000-0002-9619-3788>

## References

- [1] Hewes L 2018 World Alzheimer report 2018 *Prof. Geogr.* **2** 14–20
- [2] Li G N and Hoffman-Kim D 2008 Tissue-engineered platforms of axon guidance *Tissue Eng. B* **14** 33–51
- [3] McMurtrey R J 2014 Patterned and functionalized nanofiber scaffolds in three-dimensional hydrogel constructs enhance neurite outgrowth and directional control *J. Neural Eng.* **11** 066009
- [4] Subramanian A, Krishnan U M and Sethuraman S 2009 Development of biomaterial scaffold for nerve tissue engineering: biomaterial mediated neural regeneration *J. Biomed. Sci.* **16** 108
- [5] Boni R, Ali A, Shavandi A and Clarkson A N 2018 Current and novel polymeric biomaterials for neural tissue engineering *J. Biomed. Sci.* **25** 90
- [6] Lee J Y, Bashur C A, Goldstein A S and Schmidt C E 2009 Polypyrrole-coated electrospun PLGA nanofibers for neural tissue applications *Biomaterials* **30** 4325–35
- [7] Sill T J and von Recum H A 2008 Electrospinning: applications in drug delivery and tissue engineering *Biomaterials* **29** 1989–2006
- [8] Stepanyan R *et al* 2016 Nanofiber diameter in electrospinning of polymer solutions: Model and experiment *Polymer* **97** 428–39
- [9] Kumbar S G, James R, Nukavarapu S P and Laurencin C T 2008 Electrospun nanofiber scaffolds: engineering soft tissues *Biomed. Mater.* **3** 034002
- [10] Xie J, MacEwan M R, Schwartz A G and Xia Y 2010 Electrospun nanofibers for neural tissue engineering *Nanoscale* **2** 35–44
- [11] Yang F, Murugan R, Wang S and Ramakrishna S 2005 Electrospinning of nano/micro scale poly(L-lactic acid) aligned fibers and their potential in neural tissue engineering *Biomaterials* **26** 2603–10
- [12] Tang M, Song Q, Li N, Jiang Z, Huang R and Cheng G 2013 Enhancement of electrical signaling in neural networks on graphene films *Biomaterials* **34** 6402–11
- [13] Li N *et al* 2013 Three-dimensional graphene foam as a biocompatible and conductive scaffold for neural stem cells *Sci. Rep.* **3** 1–6
- [14] Guo W *et al* 2016 Self-powered electrical stimulation for enhancing neural differentiation of mesenchymal stem cells on graphene-poly(3,4-ethylenedioxythiophene) hybrid microfibers *ACS Nano* **10** 5086–95
- [15] Lovat V *et al* 2005 Carbon nanotube substrates boost neuronal electrical signaling *Nano Lett.* **5** 1107–10
- [16] Huang Y J, Wu H C, Tai N H and Wang T W 2012 Carbon nanotube rope with electrical stimulation promotes the

- differentiation and maturity of neural stem cells *Small* **8** 2869–77
- [17] Cellot G et al 2011 Carbon nanotube scaffolds tune synaptic strength in cultured neural circuits: novel frontiers in nanomaterial–tissue interactions *J. Neurosci.* **31** 12945–53
- [18] Lee S J et al 2018 3D printing nano conductive multi-walled carbon nanotube scaffolds for nerve regeneration *J. Neural Eng.* **15** 016018
- [19] McCaig C D, Rajnicsek A M, Song B and Zhao M 2005 Controlling cell behavior electrically: current views and future potential *Physiol. Rev.* **85** 943–78
- [20] Prochazka A 2017 Neurophysiology and neural engineering: a review *J. Neurophysiol.* **118** 1292–309
- [21] Kitchen S and Bazin S 2002 *Electrotherapy: Evidence-Based Practice* (Edinburgh: Churchill Livingstone)
- [22] Spira M E and Hai A 2013 Multi-electrode array technologies for neuroscience and cardiology *Nat. Nanotechnol.* **8** 83–94
- [23] Adly N et al 2018 Printed microelectrode arrays on soft materials: from PDMS to hydrogels *npj Flex. Electron.* **2** 1–9
- [24] Ghasemi-Mobarakeh L, Prabhakaran M P, Morshed M, Nasr-Esfahani M H and Ramakrishna S 2009 Electrical stimulation of nerve cells using conductive nanofibrous scaffolds for nerve tissue engineering *Tissue Eng. A* **15** 3605–19
- [25] Hoey J M, Lutfurakhmanov A, Schulz D L and Akhatov I S 2012 A review on aerosol-based direct-write and its applications for microelectronics *J. Nanotechnol.* **2012** 324380
- [26] Han H-V et al 2015 Resonant-enhanced full-color emission of quantum-dot-based micro LED display technology *Opt. Express* **23** 32504
- [27] Tait J G et al 2015 Uniform aerosol jet printed polymer lines with 30  $\mu\text{m}$  width for 140 ppi resolution RGB organic light emitting diodes *Org. Electron.* **22** 40–3
- [28] Mette A, Richter P L, Hörteis M and Glunz S W 2007 Metal aerosol jet printing for solar cell metallization *Prog. Photovoltaics Res. Appl.* **15** 621–7
- [29] Thompson B and Yoon H-S 2013 Aerosol-printed strain sensor using PEDOT:PSS *IEEE Sens. J.* **13** 4256–63
- [30] Adams J J et al 2011 Conformal printing of electrically small antennas on three-dimensional surfaces *Adv. Mater.* **23** 1335–40
- [31] Cho J H et al 2008 Printable ion-gel gate dielectrics for low-voltage polymer thin-film transistors on plastic *Nat. Mater.* **7** 900–6
- [32] Gupta A A, Bolduc A, Cloutier S G and Izquierdo R 2016 Aerosol jet printing for printed electronics rapid prototyping 2016 *IEEE Int. Symp. on Circuits and Systems (ISCAS)* pp 866–9
- [33] Saleh M S, Hu C and Panat R 2017 Three-dimensional microarchitected materials and devices using nanoparticle assembly by pointwise spatial printing *Sci. Adv.* **3** e1601986
- [34] Paulsen J A, Renn M, Christenson K and Plourde R 2012 Printing conformal electronics on 3D structures with aerosol jet technology 2012 *Future of Instrumentation Int. Workshop (FIIW) Proc.* pp 1–4
- [35] Wilkinson N J, Smith M A A, Kay R W and Harris R A 2019 A review of aerosol jet printing—a non-traditional hybrid process for micro-manufacturing *Int. J. Adv. Manuf. Technol.* **105** 1–21
- [36] Seifert T, Sowade E, Roscher F, Wiemer M, Gessner T and Baumann R R 2015 Additive manufacturing technologies compared: morphology of deposits of silver ink using inkjet and aerosol jet printing *Ind. Eng. Chem. Res.* **54** 769–79
- [37] Gibney R, Matthyssen S, Patterson J, Ferraris E and Zakaria N 2017 The human cornea as a model tissue for additive biomanufacturing: a review *Proc. CIRP* **65** 56–63
- [38] Grunwald I et al 2010 Surface biofunctionalization and production of miniaturized sensor structures using aerosol printing technologies *Bofabrication* **2** 014106
- [39] AEROSOL JET 300 SERIES SYSTEMS (<https://optomec.com/wp-content/uploads/2014/04/AJ-300-Systems-Web0417.pdf>)
- [40] Xu Q, Jin L, Li C, Kuddannayai S and Zhang Y 2018 The effect of electrical stimulation on cortical cells in 3D nanofibrous scaffolds *RSC Adv.* **8** 11027–35
- [41] Nunes A, Al-Jamal K, Nakajima T, Hariz M and Kostarelos K 2012 Application of carbon nanotubes in neurology: clinical perspectives and toxicological risks *Arch. Toxicol.* **86** 1009–20
- [42] Wu S, Duan B, Lu A, Wang Y, Ye Q and Zhang L 2017 Biocompatible chitin/carbon nanotubes composite hydrogels as neuronal growth substrates *Carbohydr. Polym.* **174** 830–40
- [43] Zhu L, Chang D W, Dai L and Hong Y 2007 DNA damage induced by multiwalled carbon nanotubes in mouse embryonic stem cells *Nano Lett.* **7** 3592–7
- [44] Zhang Y et al 2010 Cytotoxicity effects of graphene and single-wall carbon nanotubes in neural pheochromocytoma-derived PC12 cells *ACS Nano* **4** 3181–6
- [45] Hopley E L, Salmasi S, Kalaskar D M and Seifalian A M 2014 Carbon nanotubes leading the way forward in new generation 3D tissue engineering *Biotechnol. Adv.* **32** 1000–14
- [46] Hu H, Ni Y, Montana V, Haddon R C and Parpura V 2004 Chemically functionalized carbon nanotubes as substrates for neuronal growth *Nano Lett.* **4** 507–11
- [47] Zhang L and Webster T J 2009 Nanotechnology and nanomaterials: promises for improved tissue regeneration *Nano Today* **4** 66–80
- [48] Meng J et al 2010 Electrospun aligned nanofibrous composite of MWCNT/polyurethane to enhance vascular endothelium cells proliferation and function *J. Biomed. Mater. Res. A* **95** 312–20
- [49] Shao S et al 2011 Osteoblast function on electrically conductive electrospun PLA/MWCNTs nanofibers *Biomaterials* **32** 2821–33
- [50] Venkata K R R 2015 Conductive silver inks and their applications in printed and flexible electronics *RSC Adv.* **5** 77760–90
- [51] Pongrac I M et al 2018 Surface coating affects uptake of silver nanoparticles in neural stem cells *J. Trace Elem. Med. Biol.* **50** 684–92
- [52] Zhang X F, Liu Z G, Shen W and Gurunathan S 2016 Silver nanoparticles: synthesis, characterization, properties, applications, and therapeutic approaches *Int. J. Mol. Sci.* **17** 1534 (34 pp)
- [53] McShan D, Ray P C and Yu H 2014 Molecular toxicity mechanism of nanosilver *J. Food Drug Anal.* **22** 116–27
- [54] Baruwati B, Simmons S O, Varma R S and Veronesi B 2013 ‘Green’ synthesized and coated nanosilver alters the membrane permeability of barrier (intestinal, brain, endothelial) cells and stimulates oxidative stress pathways in neurons *ACS Sustain. Chem. Eng.* **1** 753–9
- [55] Xu F, Pieltz C, Farkas S, Qazzaz M and Syed N I 2013 Silver nanoparticles (AgNPs) cause degeneration of cytoskeleton and disrupt synaptic machinery of cultured cortical neurons *Mol. Brain* **6** 1–15
- [56] Sawicki K et al 2019 Toxicity of metallic nanoparticles in the central nervous system *Nanotechnol. Rev.* **8** 175–200
- [57] Johnston H J, Hutchison G, Christensen F M, Peters S, Hankin S and Stone V 2010 A review of the *in vivo* and *in vitro* toxicity of silver and gold particulates: particle attributes and biological mechanisms responsible for the observed toxicity *Crit. Rev. Toxicol.* **40** 328–46
- [58] Liu F et al 2015 Effects of silver nanoparticles on human and rat embryonic neural stem cells *Front. Neurosci.* **9** 1–9
- [59] Hsiao I L, Hsieh Y K, Chuang C Y, Wang C F and Huang Y J 2017 Effects of silver nanoparticles on the interactions of neuron- and glia-like cells: toxicity, uptake mechanisms, and lysosomal tracking *Environ. Toxicol.* **32** 1742–53
- [60] Repar Y N, Li H, Aguilar J S, Li Q Q, Damjana D and Hong 2017 Silver nanoparticles reduce brain inflammation and related neurotoxicity through induction of H<sub>2</sub>S-synthesizing enzymes *Sci. Rep.* **7** 1–14
- [61] Liao C, Li Y and Tjong S C 2019 Bactericidal and cytotoxic properties of silver nanoparticles *Int. J. Mol. Sci.* **20** 449
- [62] Alon N, Miroshnikov Y, Perkas N, Nissan I, Gedanken A and Shefi O 2014 Substrates coated with silver nanoparticles as a neuronal regenerative material *Int. J. Nanomed.* **9** 23–31

- [63] Ginestra P S, Madou M and Ceretti E 2019 Production of carbonized micro-patterns by photolithography and pyrolysis *Precis. Eng.* **55** 137–43
- [64] Agfa 2018 SI-AJ20x20061–25 (<https://agfa.com/specialty-products/solutions/conductive-materials/orgacon-conductive-circuitry/>)
- [65] Ferraro R M, Ginestra P S, Lanzi G, Giliani S and Ceretti E 2017 Production of micro-patterned substrates to direct Human iPSCs-derived neural stem cells orientation and interaction *Proc. CIRP* **65** pp 225–30
- [66] Ginestra P 2019 Manufacturing of polycaprolactone—graphene fibers for nerve tissue engineering *J. Mech. Behav. Biomed. Mater.* **100** 103387
- [67] Printing A and Easy M For Electronic Printing NanoJet™ Print Heads (<https://idsnm.com/nano-jet>)
- [68] Chang K A *et al* 2011 Biphasic electrical currents stimulation promotes both proliferation and differentiation of fetal neural stem cells *PLoS One* **6** e18738
- [69] Heo C *et al* 2011 The control of neural cell-to-cell interactions through non-contact electrical field stimulation using graphene electrodes *Biomaterials* **32** 19–27
- [70] Liu P, Guan R and Ye X 2013 Comparison of toxicity of uncoated and coated silver nanoparticles *J. Phys. Conf. Ser.* **429** 012025
- [71] Saleh M S *et al* 2019 CMU array: a 3D nano-printed, customizable ultra-high-density microelectrode array platform pp 1–29 accepted
- [72] Tan C P and Craighead H G 2010 Surface engineering and patterning using parylene for biological applications *Materials* **3** 1803–32